Unlocking Higher Power Efficiencies in Luminescent Solar Concentrators through Anisotropic Luminophore Emission

Julia S. van der Burgt,[§] David R. Needell,[§] Tom Veeken,[§] Albert Polman, Erik C. Garnett, and Harry A. Atwater*

ACCESS | 📊 Metrics & More | 📖 Article Recommendations

ABSTRACT: The luminescent solar concentrator (LSC) offers a potential pathway for achieving low-cost, fixed-tilt light concentration. Despite decades of research, conversion efficiency for LSC modules has fallen far short of that achievable by geometric concentrators. However, recent advances in anisotropically emitting nanophotonic structures could enable a significant step forward in efficiency. Here, we employ Monte Carlo ray-trace modeling to evaluate the conversion efficiency for anisotropic luminophore emission as a function of photoluminescence quantum yield, waveguide concentration, and geometric gain. By spanning the full LSC parameter space, we define a roadmap toward high conversion efficiency. An analytical function is derived for the dark radiative current of an LSC to calculate the conversion efficiency from the ray-tracing results. We show that luminescent concentrator conversion efficiency can be increased from the current record value of 7.1−9.6% by incorporating anisotropy. We provide design parameters for optimized luminescent solar concentrators with practical geometrical gains of 10. Using luminophores with strongly anisotropic emission and high (99%) quantum yield, we conclude that conversion efficiencies beyond 28% are achievable. This analysis reveals that for high LSC performance, waveguide losses are as important as the luminophore quantum yield.

KEYWORDS: luminescent solar concentrator, anisotropy, photovoltaics, Monte Carlo methods, nanophotonic luminophores
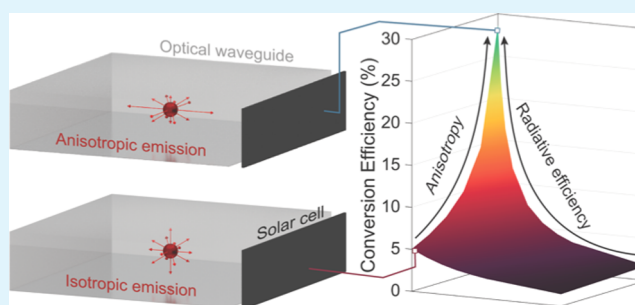
INTRODUCTION

Despite outpacing other forms of renewable energy,[1] solar photovoltaics still occupies a limited fraction of the worldwide energy portfolio—with just 580 TWh of solar electricity generated in 2019 compared to over 23 000 TWh of the total electricity consumed.[2] Given the disparity between solar generation and worldwide consumption, tremendous research effort is underway to spur further adoption. Building-integrated photovoltaics is one such area and aims to incorporate solar generation into residential and commercial building components (e.g., envelopes,[3−5] roofs,[6] windows,[7−9] greenhouses[10−14]). The decreasing cost of solar modules and the proportionate increase in the balance of system and soft costs[15] motivates the integration of photovoltaics into buildings to minimize overall system and installation expenses.[4]

First introduced in the mid-20th century for scintillation counting applications,[16] the luminescent solar concentrator (LSC) offers unique advantages for building-integrated devices. An LSC consists of a dielectric waveguide containing suspended luminophore particles at a given concentration (i.e., optical density). Upon illumination of the waveguide top surface, the embedded luminophores absorb photons within their absorption band and re-emit energetically down-shifted

photoluminescence (PL) at a radiative efficiency given by the luminophore PL quantum yield (PLQY). The spectral and angular PL emission profiles of the luminophore, along with the index of refraction contrast between the waveguide and surrounding media (often the polymer and air, respectively), determine the amount of PL trapped in the waveguide through total internal reflection (TIR). For photovoltaic applications, solar cells can be optically coupled to the waveguide edges. Figure 1a illustrates the fundamental operating principles and components of a general, single-edged photovoltaic LSC device.

Thermodynamically, an LSC holds distinct advantages over both traditional geometric concentrator modules as well as conventional, nonconcentrating photovoltaic systems. As has been shown, the Stokes shift (spectral separation between luminophore absorption and emission) sets the maximum
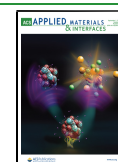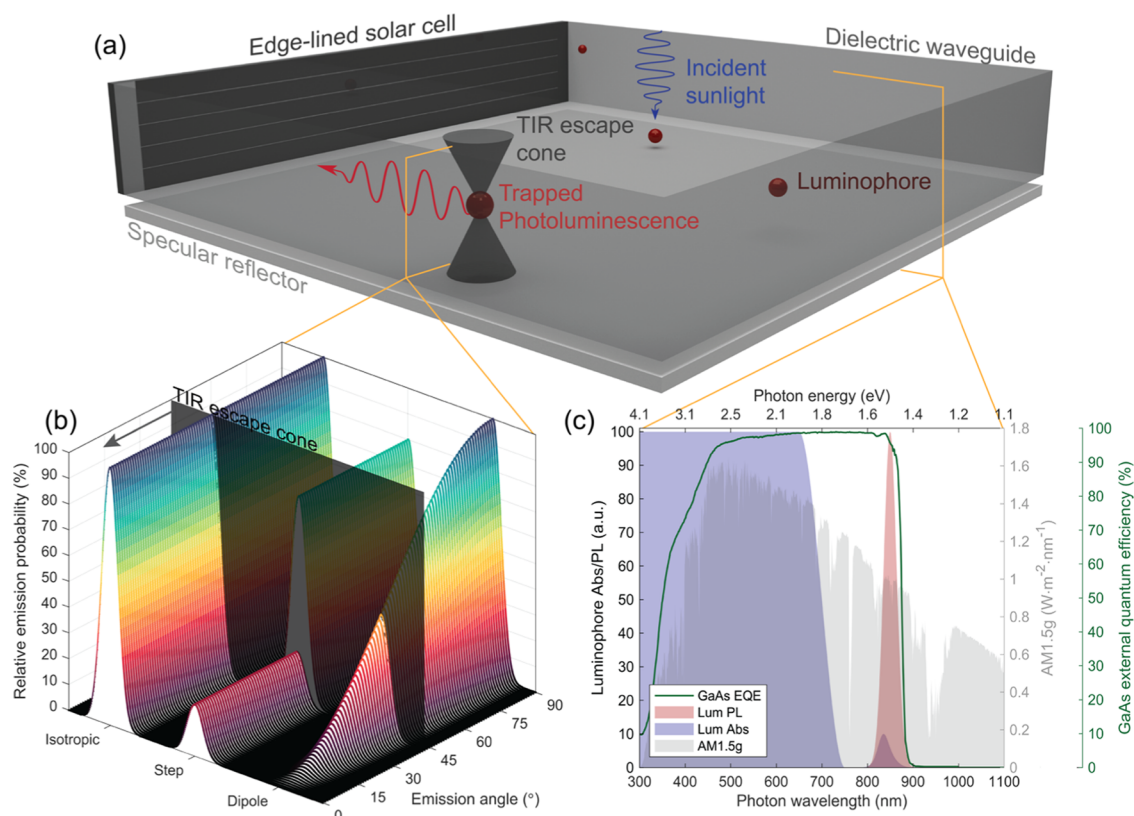
Figure 1. (a) 3D rendering of a rectangular luminescent solar concentrator coupled to an edge-lined solar PV cell. Incident sunlight strikes embedded luminophores within the optical, dielectric waveguide where, given the luminophore radiative efficiency (*i.e.*, PLQY), down-shifted PL is emitted. Given the waveguide's index of refraction, a portion of PL emits into the TIR escape cone, while a portion occupies TIR angles. In this work, we assume a waveguide with a broadband specular reflector cladding the bottom surface, as shown here. (b) Three examples of luminophore PL profiles (arbitrary wavelength) given the emission angle relative to the top waveguide surface normal. Here, we show the relative PL emission probability for the case of an isotropic luminophore with equal probability of PL across all angles; a step function like luminophore with a probability, P_{esc}, of emitting into the escape cone and a complementary probability, P_{TIR}, of emitting into TIR angles; and a dipole emission pattern showing a continuous anisotropic profile. (c) Spectral profile that we assume for this model, where we assume a luminophore with an absorption edge up to 700 nm (left *y*-axis), a PL center of 800 nm with an FWHM of 20 nm (left *y*-axis), and a GaAs cell whose external quantum efficiency (EQE) we show in green (far right *y*-axis). We plot against the AM1.5g spectrum (right *y*-axis) for reference.

achievable concentration limit.[17] Unlike traditional passive concentrators whose limit depends upon the acceptance angle,[18] LSCs can absorb and concentrate off-angle and diffuse irradiance.[19,20] Consequently, LSC photovoltaic cells maintain lower operating temperatures than both geometric concentrators and nonconcentrated, flatplate photovoltaics owing to decreased thermalization of high-energy photogenerated excitons of the collection cell.[21]

Economically, LSCs offer potential system-level cost reductions owing to the flexibility of these devices into building-integrated photovoltaic designs.[22,23] The ratio of top surface waveguide area to the net solar cell area, termed the geometric gain (GG), sets the amount of the photovoltaic material required per LSC module. The optical density of luminophores suspended within the waveguide, as well as the luminophore absorption and emission spectral profiles, determines the visible transparency and color tinting of the LSC.[24] Thus, LSCs can be aesthetically tuned to meet the need(s) of building-integrated photovoltaic designs. The LSC aesthetic tunability also compels such devices for myriad façade components and end-uses.[25,26] Beyond such applications, previous studies have also investigated routes toward high-efficiency photovoltaic applications as a promising area

for LSC research—exploring, for example, LSC–LSC[27] and LSC–Si[28−31] tandem structures.

The concentration mechanism for an LSC introduces a large number of design and performance parameters.[32] Among these include the luminophore PLQY, optical density of luminophores, GG of the LSC system, Stokes shift of the luminophore absorption/PL profiles, trapping efficiency of the emitted PL, reabsorption probability by the luminophore species, attenuation and bulk/surface scattering by the host waveguide, and the quantum efficiency of the photovoltaic cell collector.[33] Previous studies have highlighted the most important parameters for LSC optical and conversion efficiency; PLQY, PL trapping, optical density, and GG are observed to be highly influential for a given luminophore and LSC system type.[34−38] While some parameters need to be maximized (*e.g.*, PLQY) or minimized (*e.g.*, attenuation in the waveguide), others attain optimal values that strongly depend on the entire LSC design, complicating the process (*e.g.*, optical density, GG).[39,40] In addition, there exist numerous pathways for photon loss intrinsic to the LSC design. Consequently, the single-junction LSC conversion efficiency remains limited to below 10%, with the current record achieving 7.1% under 1 sun illumination.[41]

Among the many parameters that can be tuned for highly efficient LSCs, the methods by which the waveguide layer traps
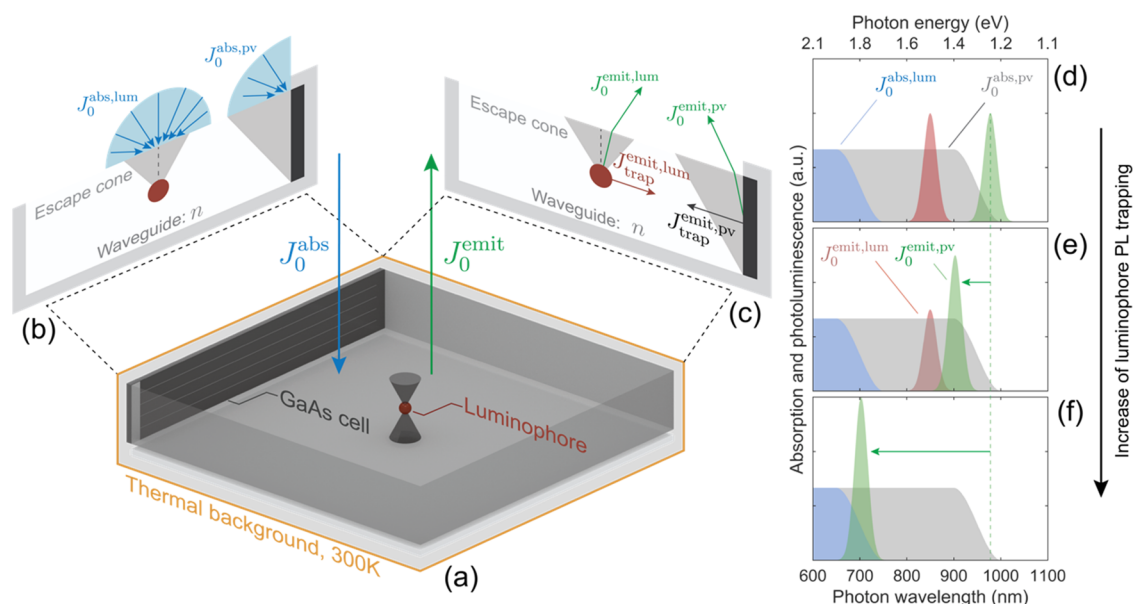
Figure 2. Conceptualization of the LSC system when in thermal equilibrium with the ambient Blackbody background at 300 K. In this case, we know that absorption into and emission out of the LSC system must be equal as shown in (a). Therefore, we can choose to analyze the system in either the absorption (b) or emission (c) pictures. (d), (e), and (f) conceptually illustrate the spectral consequence to outgoing, free space PL via the GaAs cell as the luminophore PL trapping increases. (d) depicts the case of no photoluminescence trapping, where the luminophore absorption (blue) and luminescence (red) are shown to be separated by the Stokes shift energy, and there is some spectral width to the cell PL (green) for an arbitrary cell absorption (gray). (e) and (f) show how varying the amount of luminophore PL trapping affects the spectral location of the cell emission—where, as shown in (f), complete trapping yields the highest open-circuit voltage condition, which is given by the luminophore absorption bandgap.

and guides PL to the optically coupled solar cells remain an active field of research. Common rectangular LSC waveguide materials (*e.g.*, polymer or glass) trap under 75% of the isotropically emitted luminescence radiation by TIR.[16,42] To decrease the waveguide losses through the escape cone, methods for trapping have addressed either cladding the top/bottom LSC surfaces with Bragg mirrors to reflect a portion of the PL emitted within the escape cone[43−45] or employing luminophore materials or structures that preferentially emit outside of the escape cone.[46−53] This significant body of research has detailed the effects of LSC parameters on cladding losses (*i.e.*, external dichroic mirrors and photonic crystal structures) as well as anisotropically emitting luminophores. With recent advances in the angular control of luminescence radiation using nanophotonic structures, however, this has become a key focus area for research in LSCs.[54] Together with semiconductor quantum dots whose emission efficiencies can extend beyond 99%,[55] nanophotonic-luminophore designs open new directions for improved LSC efficiency. Unlike previous works, here we quantify the effects of luminophore anisotropic emission for a variety of profiles, for a common edge-lined LSC structure, while covarying the device parameters of interest to unveil the pathway to achieving high power conversion efficiency devices.

In this work, we compare the effects of several types of anisotropic emitters on LSC conversion efficiency. Figure 1b illustrates different emission patterns for an arbitrary PL spectrum. An isotropic emitter has an equal probability of emission into any angle, as shown on the left of Figure 1b. To quantify the effects of angular emission, we model luminophores with a step-function anisotropic profile, as illustrated in the center of Figure 1b. While useful in its analysis, such a step-function emission profile is unphysical. As

such, we next discuss and analyze the consequences of more realistic, continuous emission probabilities, like that of the nanophotonic dipole emitter shown on the right-hand side of Figure 1b. We assume that the embedded luminophore particles do not anisotropically scatter incident photons below the absorption bandgap. Thus, Figure 1b displays the PL profiles of example luminophores for photons with energies greater or equal to the absorption bandgap, as given by Figure 1c. Further, unlike the absorption cross section of certain luminescent dyes that depend on their physical orientation and the angle of incidence, we assume isotropically absorbing luminophores regardless of the tilt angle within the waveguide (*e.g.*, two-dimensional transition-metal dichalcogenide hetero-bilayer absorption/emission[56] or all-dielectric resonant nano-structures coupled to quantum emitters[57,58]).

We quantify the effects of luminophore PL anisotropy in a rectangular planar LSC waveguide, employing four high-efficiency GaAs cells optically coupled to each edge of a polymer matrix. We apply an experimentally validated Monte Carlo ray-trace model to uncover the conversion efficiency performance for such an LSC employing an ideal luminophore. By evaluating the performance of the LSC with respect to power conversion efficiency (rather than, for example, concentration factor), we ensure area-agnostic comparisons across devices of differing GGs. Figure 1c highlights the external quantum efficiency (EQE) of the GaAs cell, the ideal absorption/PL spectral profiles of the luminophore, and the simulated AM1.5g irradiance assumed to strike the device at normal incidence. We include a thorough discussion of the Monte Carlo ray-trace computational method and the implementation of luminophore anisotropy within such a model. In addition, we provide a thorough physical picture of the radiative limit for such LSCs. We discuss the impact of

luminophore anisotropy on LSC performance and its covariation with PLQY, GG, and optical density. We then model the impact of luminophore PL anisotropy on the current record LSC. Finally, we end with a detailed thermodynamic breakdown of the loss mechanisms for a variety of LSCs with anisotropically emitting luminophores.

■ RESULTS AND DISCUSSION

Here, we discuss the effects of anisotropy on conversion efficiency using Monte Carlo modeling. To unveil the conversion efficiency performance with respect to luminophore anisotropy, we begin with a discussion on the LSC system detailed balance, quantifying the dark radiative current thermodynamics. Next, to consider how LSC parameters for anisotropic luminophores affect conversion efficiency, we simultaneously vary the geometric gain from 1 to 100, luminophore optical density at 750 nm from 0 to 3, and the luminophore quantum yield from 75 to 100%. We introduce the case of a steplike emission pattern and its effect on this conversion efficiency, where we vary the luminescence fraction trapped in TIR modes continuously from 75 to 100%. Finally, we analyze the LSC performance given dipole and forward emitter anisotropy profiles.

Thermodynamics of Anisotropic LSC Devices. To elucidate the conversion efficiency behavior of an arbitrary LSC device, we must quantify both the resulting short-circuit current (J_{sc}) and open-circuit voltage (V_{oc}). We can model the resulting short-circuit current density given the high accuracy Monte Carlo ray-trace methods, as described in the Computational Methods section. However, to calculate the open-circuit voltage, we first define the radiative limit case and subsequently include the GaAs cell external radiative efficiency non-idealities.[59,60] Beginning with the radiative limit equation,[61] we have

$$V_{oc}^{rad} = \frac{kT}{q} \ln\left(\frac{J_{sc}}{J_0^{rad}}\right)$$

(1)

where k, q, and T are the Boltzmann constant, electronic charge constant, and temperature of the LSC (assumed to be at 300 K), respectively. As stated, J_{sc} gives the total exciton generation under direct illumination by the sun (i.e., the short-circuit current), while J_0^{rad} gives the exciton generation under no direct illumination but instead in the ambient, Blackbody background at temperature T for purely radiative recombination and generation.

In thermodynamic equilibrium, the total absorption by the LSC system from the Blackbody background (J_0^{abs}) must equal the total emission by the LSC into free space (J_0^{emit}), as illustrated in Figure 2a. Therefore, when solving for J_0, we can choose either the absorption or emission picture.[62] Let us assume that $X\%$ of luminophore PL and $Y\%$ of GaAs PL enter the escape cone and radiate into free space. Here, $X\%$ can be calculated via the specific luminophore radiance profile—as described later in this study—and $Y\%$ by the waveguide index of refraction,[16] assumed here to be a constant 1.49 across PL wavelengths ($Y\% \cong 25\%$). Starting with the emission picture, we can distinguish the resulting LSC dark current into the contribution from the luminophore ($J_0^{emit,lum}$) and GaAs cell ($J_0^{emit,pv}$) into free space

$$J_0^{rad} = J_0^{emit} = J_0^{emit,lum} + J_0^{emit,pv}$$

(2)

Figure 2a−c conceptually illustrates this dark current term in both the emission and absorption settings. Given the $X\%$ and $Y\%$ fractions, we can rewrite eq 2 to include the total amount of the luminophore and cell emission rather than emission solely into the escape cone and thereby back into free space. Doing so, we have

$$J_0^{rad} = X\% \cdot J_{total}^{emit,lum} + Y\% \cdot J_{total}^{emit,pv}$$

(3)

where $J_{total}^{emit,lum}$ and $J_{total}^{emit,pv}$ give the total amount of PL by the luminophores and GaAs cells, respectively. Given that total absorption into the luminophores or GaAs cells must equal total emission out of the luminophores or GaAs cells, respectively, we can rewrite eq 3 in the context of the absorption profiles, as shown by Figure 1c

$$J_0^{rad} = X\% \cdot J_{total}^{abs,lum} + Y\% \cdot J_{total}^{abs,pv}$$

(4)

As shown in Figure 2b, we know that the total GaAs cell absorption ($J_{total}^{abs,pv}$) must be a sum of both the trapped luminophore PL (i.e., $1 − X\%$) and photons entering the waveguide and striking the edge-lined cell directly from the Blackbody spectrum at ambient temperature, T—where the GG gives this amount of incident light reaching the edge-lined cell. We assume, given the absorption profile of the luminophores and the fact that GaAs PLQYs are significantly lower than that of the luminophores, that the TIR-trapped GaAs PL contributes a negligible amount of the total absorption of the luminophores. Therefore, we can write

$$J_0^{rad} = X\% \cdot J_{total}^{abs,lum} + Y\% \cdot \left((1 − X\%) \cdot J_{total}^{abs,lum}\right.$$
$$\left. + \frac{1}{GG} \cdot J_0^{abs,pv}\right)$$

(5)

Where, as shown in eq 5, we distinguish between $J_{total}^{abs,lum}$ and $J_0^{abs,pv}$, where the former gives the total amount of absorption by the luminophore species—which must equal the total amount of PL—while the latter indicates the amount of irradiance absorbed by the GaAs cells exclusively from free space, Blackbody radiation and not by luminophore PL. We can now define each of these terms given our known absorption profiles and the Planck spectrum

$$J_0^{rad} = [X\% + Y\%(1 − X\%)] \cdot \int_\omega \int_\Omega A_{lum}(\omega) \cdot \Phi_{bb}(\omega) d\Omega$$
$$d\omega + Y\% \cdot \frac{1}{GG} \cdot \int_\omega \int_\Omega A_{pv}(\omega) \cdot \Phi_{bb}(\omega) d\Omega \, d\omega$$

(6)

where A_{lum} and A_{pv} are the absorption profiles of the luminophore and GaAs cell, respectively, Φ_{bb} is the Planck spectra at 300 K, ω is the frequency of the photon, and Ω is the solid angle (2π steradians for this case of background radiation). With this expression and our simulated photocurrent term from the Monte Carlo ray-trace model, we can fully define the LSC open-circuit voltage in the radiative limit. Given eq 6, we can conceptually understand the effect of luminescence trapping within a waveguide in terms of spectral shifting of the GaAs cell, highlighted by Figure 2d−f. In the limit where the geometric gain is large and the luminophores exhibit perfect PL trapping within the waveguide (i.e., $X\% = 0$), the dark radiative current is given by that of the luminophore absorption profile (that is, electronic bandgap). In this limit, the LSC open-circuit voltage is limited by the bandgap of the luminophore and not the photovoltaic cell.
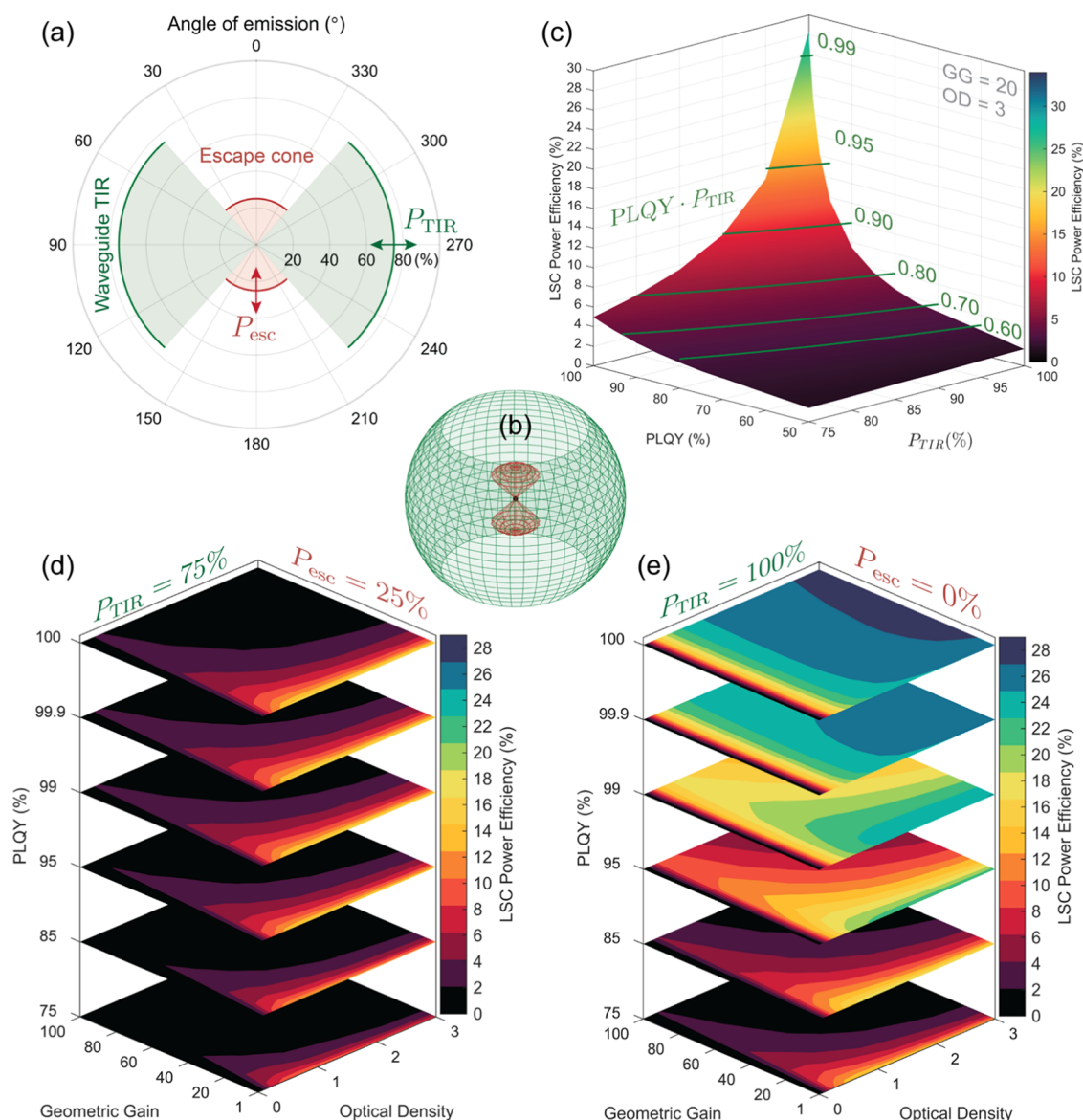
Figure 3. (a) Two-dimensional (2D) polar plot of the step-function emitter profile, illustrating how the TIR escape cone probability (P_{esc}) and TIR trapping probability (P_{TIR}) affect the overall luminescence angle of emission probability. As shown in (c), we assume symmetry about the polar angle (*i.e.*, about the *z*-axis). (b) Effects of luminophore anisotropy on the conversion efficiency of an LSC. Here, we vary the PLQY and amount of TIR emitted radiation by the luminophore, assuming a geometric gain (GG) of 20 at a waveguide optical density of 3. The analytical predictions for the waveguide efficiency (green contours) show close matching with the Monte Carlo results. (d, e) Monte Carlo ray-trace simulations for the conversion efficiency of an LSC with luminophores that emit 75% into TIR angles (*i.e.*, anisotropic) vs 100% into TIR angles (*i.e.*, anisotropic) as a function of GG, optical density, and PLQY.

As shown in Figure 2 d, if we assume general luminophore and GaAs cell absorption and emission profiles—where the luminophore absorption and PL are separated by a certain Stokes shift energy—we can qualitatively observe the impact of trapping on PL of the GaAs cell. As seen in Figure 2e, partial trapping will yield blue-shifted cell PL, while full trapping (Figure 2f) shows how the effective cell open-circuit voltage saturates to the luminophore bandgap for the limit of high GG. To include nonradiative effects of the GaAs cell, we apply an explicit form of the GaAs external radiative efficiency, as well as approximate fill factor calculations, as described in the Computational Methods section.

Emitters with Steplike Anisotropy. To begin, we assume a steplike luminescence angular emission distribution, as shown in Figure 3a,b. We vary the luminescence intensity

fraction, P_{TIR}, emitted at TIR angles, and assume this angular distribution to be symmetric about the *z*-axis (*i.e.*, normal to the waveguide plane). By representing the luminophore anisotropy with a single variable, we can uncover the relationship between anisotropic emission, GG, optical density, and PLQY. First, we vary the luminescence quantum yield and P_{TIR} of the luminophores, assuming a high optical density of 3, such that 99.9% of the incident light is absorbed in a single pass and a modest geometric gain of 20. As shown in Figure 3c, the optimal conversion efficiency occurs for unity PLQY and P_{TIR}, where for this luminophore/cell system, we observe a global maximum of approximately 29% under 1 sun illumination—approaching the detailed balance limit with respect to the luminophore absorption and reabsorption
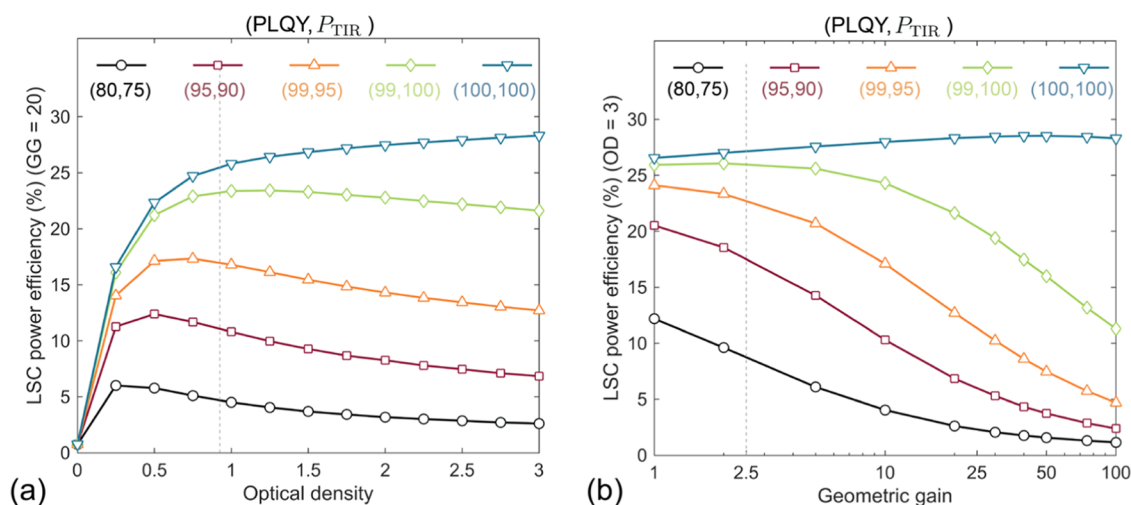
Figure 4. (a) LSC power efficiencies as a function of optical densities for several (PLQY, P_{TIR}) pairs, illustrating how an increase in the (PLQY, P_{TIR}) enables higher efficiencies and shifts the optimum OD to higher values. Here, we assume a GG of 20. (b) LSC power efficiencies as a function of GG for the same (PLQY, P_{TIR}) pairs as (a), assuming an OD of 3. We observe monotonically decreasing efficiencies with increasing GG, regardless of the PLQY and P_{TIR} due to the unavoidable surface and bulk scattering by the waveguide. The dotted lines in both (a) and (b) correspond to the OD and GG for the current record LSC with a conversion efficiency of 7.1%, respectively.
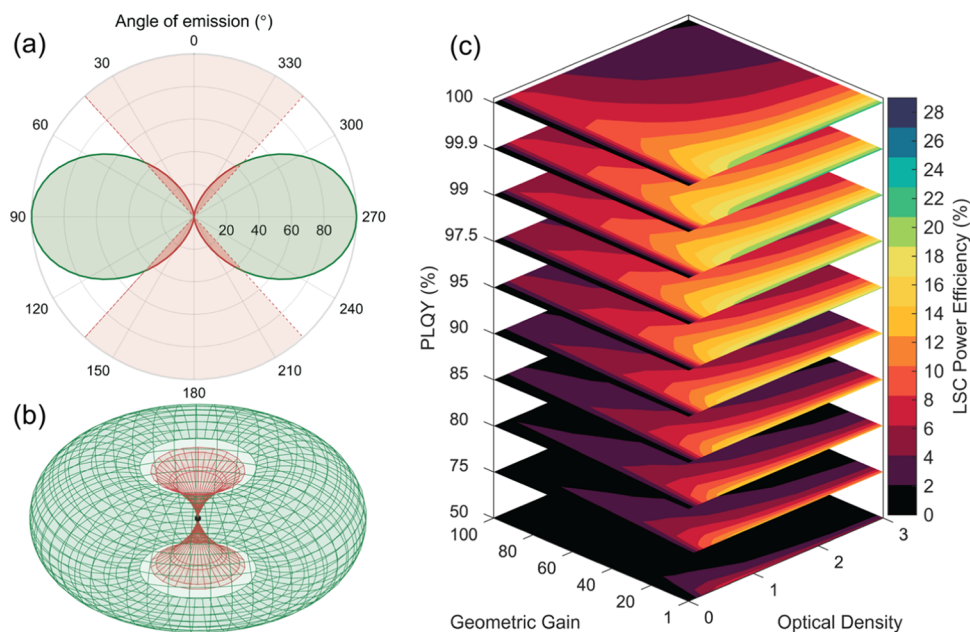

Figure 5. Monte Carlo ray-trace results for the dipolelike emission pattern, where (a) shows a polar 2D plot of the simulated PL profile with respect to the azimuthal angle and (b) illustrates the polar angle symmetry (*i.e.*, about the *z*-axis). (c) Conversion efficiency of the LSC module with respect to GG, optical density, and PLQY.

bandgaps, including nonradiative effects within the GaAs cell. In contrast, the isotropic case (P_{TIR} = 75%) falls short of 5%.

Within Figure 3c, we plot contours of the product (PLQY, P_{TIR}) for constant values of 0.60, 0.70, 0.80, 0.90, 0.95, and 0.99, finding qualitative agreement between these contours and the simulation results. This agreement can be understood from the fact that the product of luminescence quantum yield and P_{TIR} sets the probability that a trapped photon survives an absorption event by a luminophore and is guided to the solar cell. Whether the photon is lost through nonradiative recombination (for low PLQY) or by escaping the waveguide (low P_{TIR}) is irrelevant for the resulting efficiency. Significantly, increasing P_{TIR} is as important as increasing the luminescence quantum yield.

To examine the relationship between PL trapping, PLQY, GG, and optical density, Figure 3d,e shows stacked contour maps for TIR-limited and ideal trapping cases, respectively. As seen in Figure 3d, there exists a global optimum optical density for all PLQY and GG values of approximately 0.50 for PLQYs between 75 and 100%. As GG increases for PLQYs at or below 99%, we observe a steep and monotonically decreasing conversion efficiency at constant optical density. However, importantly, we find that for ideal emitters (near-unity PLQY and unity trapping) lower GG limits the maximum concentration of the system thereby constraining the open-circuit voltage to the GaAs electronic bandgap. As the GG increases for this high PLQY and trapping cases, the system
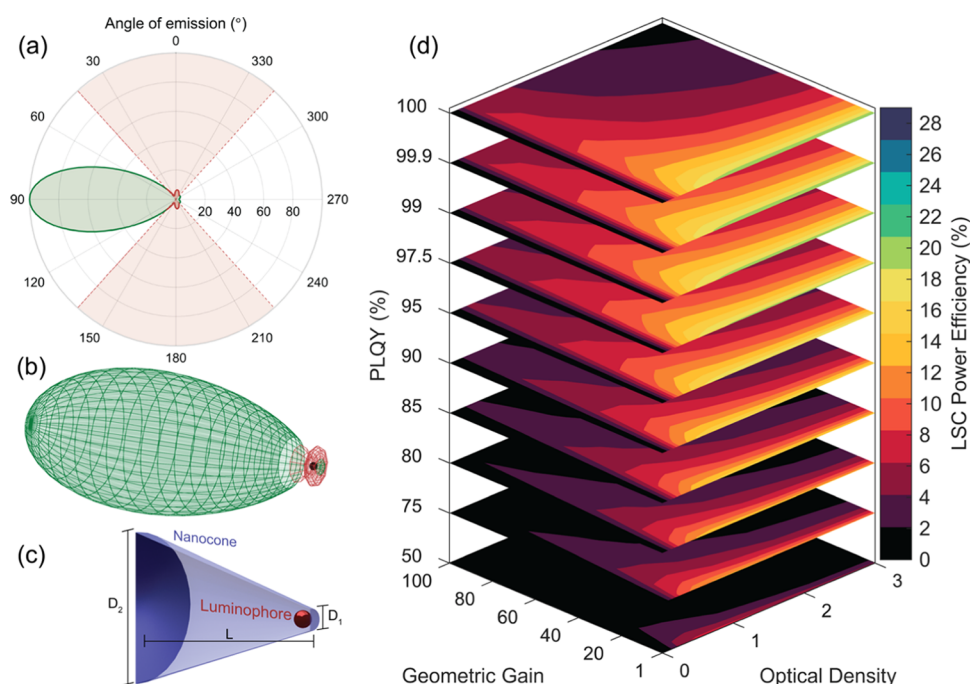
Figure 6. Monte Carlo ray-trace results for the forward, nanocone emission pattern, where (a) shows a polar 2D plot of the simulated PL profile with respect to the azimuthal angle and (b) illustrates the polar angle asymmetry of the forward emitter, where the structure preferentially emits into angles along a single direction of the horizontal x-axis. (c) 3D rendering of a cross section of the forward-emitting structure, consisting of the luminophore (red sphere) at the narrow end of the cone (R_1) of length L with a final, large radius of R_2. (d) Conversion efficiency of the LSC module with respect to GG, optical density, and PLQY.

bandgap tends toward the luminophore absorption bandgap yielding higher overall performance.

We find a similar trend with a global optimum optical density near 1.0 for cases where the PLQY falls below 95%. However, for higher PLQYs, we observe a shift in maximum conversion efficiency with respect to optical density—in the case of unity PLQY, higher optical density yields a higher conversion efficiency. Only in the case of unity trapping and unity PLQY do we observe that conversion efficiencies remain nearly constant with increasing GG. Figure 3c,e demonstrates the importance of achieving both near-unity PLQY and PL trapping.

To more closely quantify the role of optical density and GG, Figure 4a,b examines how various (PLQY, P_{TIR}) pairs impact conversion efficiency. As seen in Figure 4a, the optimal luminophore optical density depends strongly upon the waveguide trapping and luminophore radiative efficiency. Since this density determines both the amount of absorbed sunlight as well as the amount of PL reabsorption within the waveguide, a poor PLQY and P_{TIR} results in detrimental nonradiative recombination and high escape cone losses for the absorbed incident and re-emitted PL photons. As the (PLQY, P_{TIR}) product increases, the drawback of reabsorption diminishes while the advantage of increased sunlight absorption remains, thereby increasing the optimal optical density. Figure 4b illustrates the difficulty in achieving a high conversion efficiency for the increasingly large waveguide to cell area ratios for products less than unity. In all but the ideal case, efficiency monotonically decreases with increasing GG. Even in this special case of unity PLQY and P_{TIR}, increasing the GG beyond a certain value yields higher likelihood of photoluminescence scattering inside the escape cone, resulting in lowered conversion efficiencies. For efficiencies above 15%

at GGs above 10, the (PLQY, P_{TIR}) product must be greater than 85%. Having demonstrated the upper performance limits of the LSC with a steplike emission profile, we can readily observe the interplay between the various LSC parameters as well as quantify how to reach increased power conversion efficiencies. However, to understand the limitations of more experimental anisotropic profiles, we next discuss several more realistic emission patterns.

Emitters with Dipolelike Anisotropy. For a more realistic approximation of a luminescent concentrator employing anisotropic emission, we model a system comprised of dipolelike emitters. Figure 5a,b illustrates the polar and 3D plots of the far-field dipole emission pattern, where we again observe symmetry about the z-axis. We find upon integration that approximately 91% of the generated luminescence is emitted into TIR angles. Varying the PLQY, GG, and optical density, we find that—similar to our previous analysis for nonunity (PLQY, P_{TIR}) pairs—there exist optimal optical densities. A PLQY of 95% and GGs below 60 yield optimal optical densities of approximately 0.67. We find maximum conversion efficiency of approximately 25% for the case of unity PLQY, an optical density of 3, and GG of 1. For a GG of 10, a geometry of practical experimental interest, the maximum conversion efficiency is approximately 18.5% for unity PLQY and an optical density of 0.75.

Emitters with Forwardlike Anisotropy. Thus far, our analysis has employed anisotropic emitters with far-field radiation symmetric about the z-axis. We now turn attention to optical structures that exhibit strong emission in a single direction, breaking this symmetry. In the case of emission systems symmetric about the z-axis, photons perform random walks throughout the waveguide. By contrast, forward-emitting luminophores exhibit a decreased mean free path for photon
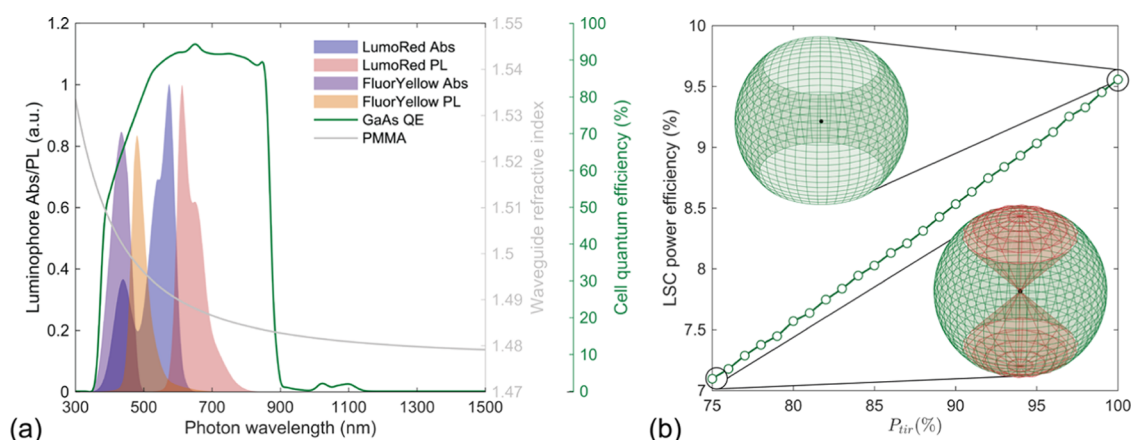
Figure 7. (a) Spectral characteristics of the current record LSC device, consisting of two luminophores within the waveguide (Lumogen Red, Fluorescence Yellow) (left y-axis), four edge-lined GaAs cells (cell quantum efficiency at far right y-axis), and a PMMA waveguide matrix (refractive index at right y-axis). (b) Monte Carlo ray-trace simulations showing the impact of anisotropy on the conversion efficiency for the current record device. At the isotropic limit (P_{TIR} of 75%), we observe close matching between measured and modeled efficiencies (7.1% measured and 7.096% modeled). At the anisotropic limit, power efficiencies reach 9.6%, a relative increase of approximately 35%.

propagation to the collector cells. As detailed in the Methods section, we simulate forward-emitting luminophores consisting of spherical absorbing/emitting nanoparticles embedded within a nanocone. For such a forward-emitting luminophore, Figure 6a−c highlights the polar radiation plot, spatial radiation profile, and nanocone structure. Integrating the luminescence intensity, we observe that approximately 88% of the intensity from such structures couples into the TIR waveguide angles—slightly less than for the dipole emitter.

As shown in Figure 6d, the dependence of forward emitter conversion efficiency on optical density, GG, and PLQY closely parallels that of the dipole emitter case. However, even though the forward emitter is 33% more likely to emit photons into the escape cone relative to dipole structures, we observe a maximum conversion efficiency of 24%, approximately 96% of the dipole emitter maximum. We find fewer luminescence reabsorption events for forward emitters compared to their dipole emitter counterparts, suggesting that breaking this z-axis symmetry enables shorter luminescence mean free paths within the waveguide. This shorter path almost completely compensates the increased escape cone loss. Further, we observe that for a GG of 10, the maximum conversion efficiency reaches 17.3% for the case of unity PLQY and an optical density of 0.75.

Enhancing the efficiency of the Record LSC. While the dipole and forward emission cases correspond to physically realizable emitters, the LSC structure itself assumes certain idealities. Specifically, we thus far have assumed record GaAs PV cells coupled to ideal luminophore emitters with a narrow PL profile matched to the GaAs bandgap (as shown in Figure 1c). Additionally, our simulated LSC waveguide matrix assumes a constant index of refraction for generated PL. To illustrate how anisotropic emission can significantly benefit less idealized systems, we model the current record conversion efficiency LSC fabricated by Slooff et al.[63] As shown in Figure 7a, this device employs two luminophore species: Lumogen Red and Fluorescence Yellow dyes, with peak optical densities of 0.71 and 2.36, and luminescence quantum yields of 87 and 98%, respectively. With a square waveguide side length of 5 cm and an overall thickness of 0.50 cm, the fabricated LSC yields an overall GG of 2.5. Figure 7a displays the refractive index of the waveguide polymer matrix material, poly(methyl meth-

acrylate), as well as the external quantum efficiency of the GaAs solar cell. Finally, a diffuse Lambertian-scattering back reflector is coupled to the bottom surface of the waveguide, with approximately 97% averaged reflectance at PL wavelengths.

We first simulate this record efficiency LSC and validate our model by obtaining conversion efficiencies equal to the experimental measurement. As a next step, we systematically vary the luminescence fraction emitted into TIR angles in the waveguide. As shown in Figure 7b, the isotropic emission case (i.e., P_{TIR} of 75%) attains the experimentally measured conversion efficiency value of 7.1% under 1 sun illumination. However, upon increasing the anisotropic luminescence fraction, we find a monotonic increase in performance up to 9.6% in the ideal case of unity P_{TIR}——a relative increase of 35%. The observed conversion efficiency enhancement resulting from luminophore anisotropy underscores the crucial role waveguide trapping plays in enabling high conversion efficiency.

Loss Mechanisms within Anisotropic LSCs. As discussed in the Methods section, we track photons collected as well as photons lost. For the luminescent concentrator, we categorize losses into five thermodynamic mechanisms. Figure 8a−c illustrates these losses as a function of the luminophore optical density at an LSC GG of 20, assuming PLQY of 95%. For each of the three emitter types (step, dipole, and forward), losses can be understood as either: (i) nonabsorbed incident photons, either due to sub-bandgap photon energy or low luminophore optical density; (ii) thermalization, i.e., energetic relaxation of photogenerated excitons to the luminophore bandgap energy; (iii) waveguide escape cone loss; (iv) subunity PLQY loss; and (v) loss from the photovoltaic cell itself, owing to thermalization from the luminophore emission energy to the cell bandgap, subunity collection efficiencies (i.e., EQE), fill factor, and cell contact resistance.

Figure 8a−c illustrates the trade-off between optical density and maximum conversion efficiency (black). Although a higher optical density minimizes the nonabsorbed incident light (blue), waveguide escape cone loss (yellow) and luminophore nonradiative recombination (orange) adversely affect the overall performance for the dipole and forward emitters. For the perfect step emitter, we observe that increased
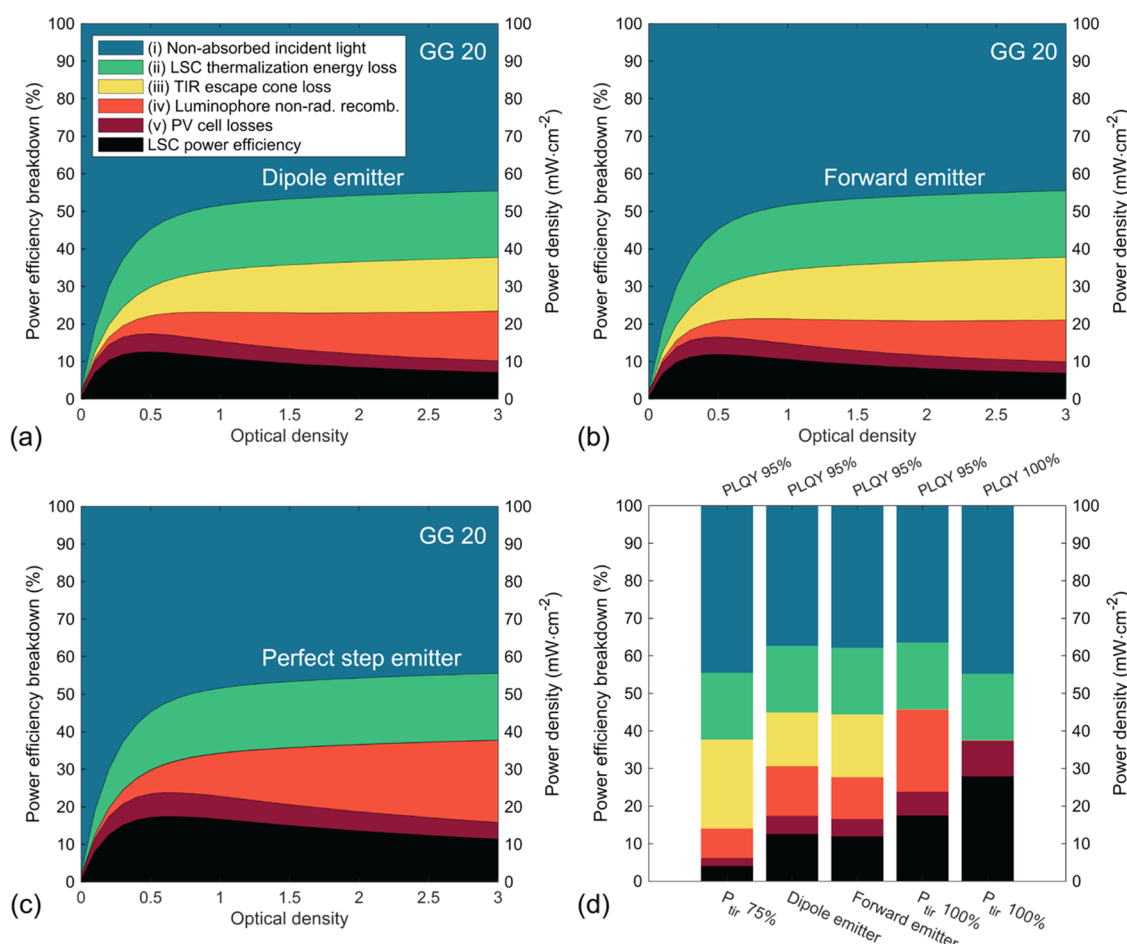
Figure 8. Overall conversion efficiency loss mechanisms of an LSC with respect to the optical density of the luminophores within the optical waveguide for the case of the dipole emitter (a), forward emitter (b), and perfect anisotropic step emitter (c). (a), (b), and (c) assume a PLQY of 95%. Here, we define the losses as (i) incident irradiance not absorbed by the LSC, limited by both the absorption spectrum of the luminophore and, for lower optical densities, the amount of in-band luminophore absorption; (ii) LSC thermalization energy loss, owing to the thermalization of photogenerated excitons within the luminophore that relax to the PL band; (iii) TIR escape cone loss of the PL, which can result from emitted PL coupling into the cone from an emission event or a scattering event by the waveguide; (iv) luminophore nonradiative recombination of photogenerated excitons given nonunity PLQYs; and (v) PV cell losses, which include parasitic absorption, given the limited internal quantum efficiency of the coupled cell material and thermalization from the PL emission wavelength to the bandgap of the cell. (d) Comparison of five cases at optimal OD given the emitter and GG of 20 for (from left to right): a PLQY of 95% and TIR-limited PL trapping, the dipole emitter at 95% PLQY, the forward emitter at 95% PLQY, a PLQY of 95% and perfect PL trapping, and the upper performance limit of unity PLQY and perfect PL trapping.

luminophore optical density yields substantially higher amounts of luminophore nonradiative recombination (orange). As expected, we observe lower escape cone loss in the dipole emitter case compared to that of the forward emitter. However, the forward emitter loses comparatively less power through luminophore nonradiative recombination compared to the dipole case given shorter mean free PL path lengths, as previously discussed.

Figure 8d compares four nonideal systems to an ideal case of unity PLQY and P_{TIR}, a high optical density of 3, and a GG of 20 (yielding a maximum conversion efficiency of approximately 29%). For isotropic emission (*i.e.*, P_{TIR} of 75%) at a PLQY of 95%, the dominant loss mechanism is PL coupling into the escape cone. We also observe that for dipole, forward, or perfect step emission and PLQY of 95%, the primary loss mechanism is luminophore nonradiative recombination. In the ideal case of complete PL trapping and perfect luminophore radiative efficiency, the LSC conversion efficiency reaches the detailed balance limit of a photovoltaic system whose bandgap

is given by the luminophore absorption spectra rather than the GaAs bandgap. This can be understood given that incident light with energies greater than the bandgap of the cell, but less than the luminophore absorption edge, will not be absorbed by either the luminophore or waveguide matrix—assuming a dielectric waveguide with an arbitrarily large bandgap (*i.e.*, insulator). As demonstrated by previous studies,[64,65] LSCs can retain the detailed balance limit only if this condition holds where the dark radiative saturation current is not scaled with the short-circuit current.

■ CONCLUSIONS AND FUTURE WORK

In this work, we investigate the role that anisotropy plays in improving LSC conversion efficiency. Through Monte Carlo simulations, we illustrate the importance of maximizing the waveguide trapping efficiency, P_{TIR}, in addition to the luminophore radiative efficiency, PLQY. By systematic variation of critical design parameters, we explore the role of anisotropic luminophore emission for ideal step, dipole, and

forward emitters on LSC conversion efficiency. We find that for the experimental luminophores and LSC design used for the present record LSC (conversion efficiency 7.1%), the upper anisotropic emission limit (P_{TIR} = 100%) increases this efficiency to 9.6%. Our model also shows that a modest geometrical gain (GG = 10) can be realized with a conversion efficiency of greater than 15% via anisotropic luminophore emission (P_{TIR} = 95%) with a luminescence quantum yield of 99%. Notably, a conversion efficiency above 25% is achievable for PLQY = 99% and full light trapping (P_{TIR} = 100%) at such a geometric gain. The recent demonstration of luminophores with ultrahigh luminescence quantum yield, combined with well-developed nanophotonics design and fabrication methods for anisotropic scatterers, can open the door to previously unreachable LSC conversion efficiencies.

■ COMPUTATIONAL METHODS

We employ a Monte Carlo ray-trace model to evaluate LSC conversion efficiency for varying GG, luminophore optical density, PLQY, and PL emission patterns. Previous studies have validated this model both with experimental data and also LSCs reported in the literature.[66] The Monte Carlo stochastically traces individual photons throughout each layer of the LSC. We initialize a constant grid matrix across the waveguide top surface area of 150 by 150 for all GGs, simulating photon wavelengths between 300 and 1200 nm in steps of 10 nm. Following the previous methods,[67] we model approximately 2 × 10^6 photons for each LSC module type to achieve statistically reliable results. We adopt an ideal luminophore absorption and PL profile with a Stokes shift of approximately 200 nm from the absorption edge (750 nm) to the PL center (950 nm). Each luminophore exhibits reabsorption, as shown in Figure 1c. We base the luminophore absorption band tail and PL full width at half maximum archetype core/shell quantum dot structures.

We track the photon's previous and current positions (x, y, z), previous and current velocity vectors (v_x, v_y, v_z), and original and current wavelengths (λ_0, λ). Photons propagate through the LSC in discrete steps of 5 μm, where the current velocity determines the resulting direction. To determine the probability of luminophore absorption, we apply the Beer–Lambert law, given the optical density constant of that particular LSC for a given simulation step. To determine reflection and refraction angles at LSC layer interfaces, we apply Fresnel and Snell laws, respectively, for an assumed waveguide with a refractive index of 1.49 at the PL emission wavelengths, approximately 800–900 nm. We model current record high-efficiency Alta Devices' GaAs cells and simulate the photon–cell interaction through the measured reflectance and internal quantum efficiency, where we assume 2.5% of the cell surface area to be entirely reflective, representative of the front metal contact area. We assume GaAs edge-lined cells to optically couple to each of the four perimeter edges of 100 μm thick LSC waveguides, where we set the edge length according to the GG (GG of 1 corresponds to a 400 μm perimeter). We assume a perfect specular back reflector optically coupled to the bottom surface of the LSC to evaluate escape cone loss for only the top waveguide surface.

For each photon striking the LSC, we mark whether the photon is collected by one of the four edge-lined GaAs cells or lost via a particular mechanism. If collected, we weigh the original incident photon wavelength by the AM1.5G solar spectrum to calculate the resulting photocurrent density of a given GaAs cell. We assume the four GaAs cells to be connected in parallel. Once all photons are simulated and determined, collected or lost, we calculate the open-circuit voltage and fill factor. To calculate the former, we assume an arbitrarily large dielectric waveguide electronic bandgap, such that any contribution from the waveguide matrix to the radiative dark saturation current of the GaAs cell is negligible. We then calculate the radiative limit open-circuit voltage given the absorption spectra of the luminophore—scaling by the luminophore optical density and the emission out of the waveguide and into the escape cone. We also consider the contribution to the radiative dark current via background spectra photons reaching the GaAs cells directly—scaling by the system GG and emission out of the waveguide given by the refractive index. To account for cell nonradiative combination of photogenerated excitons, we apply an explicit approximation within such GaAs cells, as given by eq 7.[60] Finally, we calculate the fill factor given previous explicit models that have shown close experimental matching and apply series and shunt resistances to match the diode behavior for current, record GaAs cells.[68]

$$V_{oc}^{nonrad} = \frac{kT}{q} \ln\left(\frac{2.5}{1 + 1/J_{sc}} \right) \quad (7)$$

To vary the angular distribution of emission for embedded luminophores, we generate a probability distribution function for each radiation pattern (i.e., a steplike, dipolelike, and forwardlike emission). We assume a uniform alignment of all luminophore emitters within the waveguide. The step emission profile, as depicted in Figure 1b, assumes a constant probability of emission for angles inside the escape cone for a waveguide refractive index of 1.49. We employ a dipole emission profile following previous studies of the emission angle.[69]

Finally, we model directional forward radiation to evaluate the LSC performance for a luminophore whose angular distribution is anisotropic in both the azimuthal and polar directions. Here, we assume a nanocone structure of a refractive index 2.5 hosting an embedded spherical luminophore. We performed full-wave electromagnetic simulations using the finite-difference time-domain (FDTD) method to model the far-field radiation pattern. In the full-wave simulations, we varied the nanocone central axis length, front and end radii, and emitter position along the central axis. We implemented a particle swarm optimization routine within this four-dimensional design space (i.e., axis length, front radius, end radius, emitter position) to probe the optimal performing structure, where the fraction of emission into the forward direction is taken as the figure of merit. The champion structure has an 887 nm axis length and radii of 180 and 1367 nm.

■ AUTHOR INFORMATION

Corresponding Author

Harry A. Atwater − *Department of Applied Physics and Materials Science, California Institute of Technology, Pasadena, California 91125, United States;* ⊙ orcid.org/0000-0001-9435-0201; Email: haa@caltech.edu

Authors

Julia S. van der Burgt − *Center for Nanophotonics, NWO-Institute AMOLF, 1098XG Amsterdam, The Netherlands*

David R. Needell − *Department of Applied Physics and Materials Science, California Institute of Technology, Pasadena, California 91125, United States*

Tom Veeken − *Center for Nanophotonics, NWO-Institute AMOLF, 1098XG Amsterdam, The Netherlands*

Albert Polman − *Center for Nanophotonics, NWO-Institute AMOLF, 1098XG Amsterdam, The Netherlands;* ⊙ orcid.org/0000-0002-0685-3886

Erik C. Garnett − *Center for Nanophotonics, NWO-Institute AMOLF, 1098XG Amsterdam, The Netherlands;* ⊙ orcid.org/0000-0002-9158-8326

Complete contact information is available at:
https://pubs.acs.org/10.1021/acsami.1c12547

Author Contributions

§J.S.v.d.B., D.R.N., and T.V. contributed equally to this work.

Notes

The authors declare no competing financial interest.

■ REFERENCES

(1) BP. BP Statistical Review of World Energy. https://www.bp.com/content/dam/bp/business-sites/en/global/corporate/pdfs/energy-economics/statistical-review/bp-stats-review-2020-full-report.pdf (accessed July 15th, 2021).

(2) Enerdata. Global Energy Statistical Yearbook. https://yearbook.enerdata.net/electricity/electricity-domestic-consumption-data.html (accessed July 15th, 2021).

(3) Meir, M. *State-of-the-Art and SWOT Analysis of Building Integrated Solar Envelope Systems*; Bonato, P.; Fedrizzi, R.; D'Antoni, M., Eds.; 2019.

(4) Yang, R. J.; Zou, P. X. W. Building Integrated Photovoltaics (BIPV): Costs, Benefits, Risks, Barriers and Improvement Strategy. *Int. J. Constr. Manage.* 2016, 16, 39−53.

(5) Kuhn, T. E.; Erban, C.; Heinrich, M.; Eisenlohr, J.; Ensslen, F.; Neuhaus, D. H. Review of Technological Design Options for Building Integrated Photovoltaics (BIPV). *Energy Build.* 2020, No. 110381.

(6) Kryszak, M.; Wang, L. W. The Value of Aesthetics in the BIPV Roof Products Segment: A Multiperspective Study under European Market Conditions. *Energy Sources, Part A* 2020, 1−22.

(7) Lunt, R. R.; Bulovic, V. Transparent, near-Infrared Organic Photovoltaic Solar Cells for Window and Energy-Scavenging Applications. *Appl. Phys. Lett.* 2011, 98, No. 113305.

(8) Traverse, C. J.; Pandey, R.; Barr, M. C.; Lunt, R. R. Emergence of Highly Transparent Photovoltaics for Distributed Applications. *Nat. Energy* 2017, 2, 849−860.

(9) Husain, A. A. F.; Hasan, W. Z. W.; Shafie, S.; Hamidon, M. N.; Pandey, S. S. A Review of Transparent Solar Photovoltaic Technologies. *Renewable Sustainable Energy Rev.* 2018, 94, 779−791.

(10) Lamnatou, C.; Chemisana, D. Solar Radiation Manipulations and Their Role in Greenhouse Claddings: Fluorescent Solar Concentrators, Photoselective and Other Materials. *Renewable Sustainable Energy Rev.* 2013, 27, 175−190.

(11) Weber, W. H. H.; Lambe, J. Luminescent Greenhouse Collector for Solar Radiation. *Appl. Opt.* 1976, 15, 2299.

(12) Corrado, C.; Leow, S. W.; Osborn, M.; Carbone, I.; Hellier, K.; Short, M.; Alers, G.; Carter, S. A. Power Generation Study of Luminescent Solar Concentrator Greenhouse. *J. Renewable Sustainable Energy* 2016, 8, No. 043502.

(13) Loik, M. E.; Carter, S. A.; Alers, G.; Wade, C. E.; Shugar, D.; Corrado, C.; Jokerst, D.; Kitayama, C. Wavelength-Selective Solar Photovoltaic Systems: Powering Greenhouses for Plant Growth at the Food-Energy-Water Nexus. *Earth's Future* 2017, 5, 1044−1053.

(14) Cuce, E.; Harjunowibowo, D.; Cuce, P. M. Renewable and Sustainable Energy Saving Strategies for Greenhouse Systems: A Comprehensive Review. *Renewable Sustainable Energy Rev.* 2016, 64, 34−59.

(15) Fu, R.; Feldman, D.; Margolis, R.; Woodhouse, M.; Ardani, K.; Fu, R.; Feldman, D.; Margolis, R.; Woodhouse, M.; Ardani, K. U. S. *US Solar Photovoltaic System Cost Benchmark: Q1 2018*; National Renewable Energy Laboratory (NREL): Golden, CO, 2018.

(16) Shurcliff, W. A.; Jones, C. R. The Trapping of Fluorescent Light Produced within Objects of High Geometrical Symmetry. *J. Opt. Soc. Am.* 1949, 39, 912−916.

(17) Yablonovitch, E. Thermodynamics of the Fluorescent Planar Concentrator. *J. Opt. Soc. Am.* 1980, 70, 1362−1363.

(18) Rabl, A. Comparison of Solar Concentrators. *Sol. Energy* 1976, 18, 93−111.

(19) Debije, M. G.; Rajkumar, V. A. Direct versus Indirect Illumination of a Prototype Luminescent Solar Concentrator. *Sol. Energy* 2015, 122, 334−340.

(20) Li, Y.; Sun, Y.; Zhang, Y. Luminescent Solar Concentrators Performing under Different Light Conditions. *Sol. Energy* 2019, 188, 1248−1255.

(21) Rajkumar, V. A.; Weijers, C.; Debije, M. G. Distribution of Absorbed Heat in Luminescent Solar Concentrator Lightguides and Effect on Temperatures of Mounted Photovoltaic Cells. *Renewable Energy* 2015, 80, 308−315.

(22) Reinders, A.; Kishore, R.; Slooff, L.; Eggink, W. Luminescent Solar Concentrator Photovoltaic Designs. *Jpn. J. Appl. Phys.* 2018, 57, No. 08RD10.

(23) Moraitis, P.; Leeuwen, G.; Sark, W. Visual Appearance of Nanocrystal-Based Luminescent Solar Concentrators. *Materials* 2019, 12, 885.

(24) Meinardi, F.; Bruni, F.; Brovelli, S. Luminescent Solar Concentrators for Building-Integrated Photovoltaics. *Nat. Rev. Mater.* 2017, 2, No. 17072.

(25) Reinders, A.; Debije, M. G.; Rosemann, A. Measured Efficiency of a Luminescent Solar Concentrator PV Module Called Leaf Roof. *IEEE J. Photovoltaics* 2017, 7, 1663−1666.

(26) Sol, J. A. H. P.; Timmermans, G. H.; van Breugel, A. J.; Schenning, A. P. H. J.; Debije, M. G. Multistate Luminescent Solar Concentrator "Smart" Windows. *Adv. Energy Mater.* 2018, 8, No. 1702922.

(27) Wu, K.; Li, H.; Klimov, V. I. Tandem Luminescent Solar Concentrators Based on Engineered Quantum Dots. *Nat. Photonics* 2018, 12, 105−110.

(28) Needell, D. R.; Ilic, O.; Bukowsky, C. R.; Nett, Z.; Xu, L.; He, J.; Bauser, H.; Lee, B. G.; Geisz, J. F.; Nuzzo, R. G.; Alivisatos, A. P.; Atwater, H. A. Design Criteria for Micro-Optical Tandem Luminescent Solar Concentrators. *IEEE J. Photovoltaics* 2018, 8, 1560−1567.

(29) Needell, D. R.; Nett, Z.; Ilic, O.; Bukowsky, C. R.; He, J.; Xu, L.; Nuzzo, R. G.; Lee, B. G.; Geisz, J. F.; Alivisatos, A. P.; Atwater, H. A. Micro-Optical Tandem Luminescent Solar Concentrator. In *2017 IEEE 44th Photovoltaic Specialist Conference (PVSC)*; IEEE, 2017; pp 1737−1740.

(30) Needell, D. R.; Bukowsky, C. R.; Darbe, S.; Bauser, H.; Ilic, O.; Atwater, H. A. Spectrally Matched Quantum Dot Photoluminescence in GaAs-Si Tandem Luminescent Solar Concentrators. *IEEE J. Photovoltaics* 2019, 9, 397−401.

(31) Lunardi, M. M.; Needell, D. R.; Bauser, H.; Phelan, M.; Atwater, H. A.; Corkish, R. Life Cycle Assessment of Tandem LSC-Si Devices. *Energy* 2019, 181, 1−10.

(32) Debije, M. G.; Verbunt, P. P. C. Thirty Years of Luminescent Solar Concentrator Research: Solar Energy for the Built Environment. *Adv. Energy Mater.* 2012, 2, 12−35.

(33) Goetzberger, a.; Greubel, W. Applied Physics Solar Energy Conversion with Fluorescent Collectors. *Appl. Phys.* 1977, 14, 123−139.

(34) Tummeltshammer, C.; Taylor, A.; Kenyon, A. J.; Papakonstantinou, I. Losses in Luminescent Solar Concentrators Unveiled. *Sol. Energy Mater. Sol. Cells* 2016, 40.

(35) Burgers, a. R.; Slooff, L. H.; Kinderman, R.; Roosmalen, J. A. M. v. In Modeling of Luminescent Concentrators by Ray-Tracing, *20th European Photovoltaic Solar Energy Conference and Exhibition*, 2005; p 10.

(36) Rowan, B. C.; Wilson, L. R.; Richards, B. S. Advanced Material Concepts for Luminescent Solar Concentrators. *IEEE J. Sel. Top. Quantum Electron.* 2008, 14, 1312−1322.

(37) Martínez, A. L.; Gómez, D. Design, Fabrication, and Characterization of a Luminescent Solar Concentrator with Optimized Optical Concentration through Minimization of Optical Losses. *J. Photonics Energy* **2016**, *6*, No. 045504.

(38) Krumer, Z.; van Sark, W. G. J. H. M.; Schropp, R. E. I.; de Mello Donegá, C. Compensation of Self-Absorption Losses in Luminescent Solar Concentrators by Increasing Luminophore Concentration. *Sol. Energy Mater. Sol. Cells* **2017**, *167*, 133−139.

(39) Kerrouche, A.; Hardy, D. A.; Ross, D.; Richards, B. S. Luminescent Solar Concentrators: From Experimental Validation of 3D Ray-Tracing Simulations to Coloured Stained-Glass Windows for BIPV. *Sol. Energy Mater. Sol. Cells* **2014**, *122*, 99−106.

(40) Connell, R.; Pinnell, C.; Ferry, V. E. Designing Spectrally-Selective Mirrors for Use in Luminescent Solar Concentrators. *J. Opt.* **2018**, *20*, No. 024009.

(41) Slooff, L. H.; Bende, E. E.; Burgers, A. R.; Budel, T.; Pravettoni, M.; Kenny, R. P.; Dunlop, E. D.; Buchtemann, A. A Luminescent Solar Concentrator with 7.1% Power Conversion Efficiency. *Phys. Status Solidi RRL* **2008**, *2*, 257−259.

(42) Debije, M. G.; Evans, R. C.; Griffini, G. Laboratory Protocols for Measuring and Reporting the Performance of Luminescent Solar Concentrators. *Energy Environ. Sci.* **2021**, *14*, 293−301.

(43) Xu, L.; Yao, Y.; Bronstein, N. D.; Li, L.; Alivisatos, A. P.; Nuzzo, R. G. Enhanced Photon Collection in Luminescent Solar Concentrators with Distributed Bragg Reflectors. *ACS Photonics* **2016**, *3*, 278−285.

(44) de Boer, D. K. G.; Broer, D. J.; Debije, M. G.; Keur, W.; Meijerink, A.; Ronda, C. R.; Verbunt, P. P. C. Progress in Phosphors and Filters for Luminescent Solar Concentrators. *Opt. Express* **2012**, *20*, A395.

(45) de Boer, D. K. G.; Lin, C.-W.; Giesbers, M. P.; Cornelissen, H. J.; Debije, M. G.; Verbunt, P. P. C.; Broer, D. J. Polarization-Independent Filters for Luminescent Solar Concentrators. *Appl. Phys. Lett.* **2011**, *98*, No. 021111.

(46) Tummeltshammer, C.; Taylor, A.; Kenyon, A. J.; Papakonstantinou, I. Homeotropic Alignment and Förster Resonance Energy Transfer: The Way to a Brighter Luminescent Solar Concentrator. *J. Appl. Phys.* **2014**, *116*, No. 173103.

(47) Debije, M. G. Solar Energy Collectors with Tunable Transmission. *Adv. Funct. Mater.* **2010**, *20*, 1498−1502.

(48) Mulder, C. L.; Reusswig, P. D.; Beyler, A. P.; Kim, H.; Rotschild, C.; Baldo, M. A. Dye Alignment in Luminescent Solar Concentrators: II Horizontal Alignment for Energy Harvesting in Linear Polarizers. *Opt. Express* **2010**, *18*, A91.

(49) Bauser, H. C.; Bukowsky, C. R.; Phelan, M.; Weigand, W.; Needell, D. R.; Holman, Z. C.; Atwater, H. A. Photonic Crystal Waveguides for>90% Light Trapping Efficiency in Luminescent Solar Concentrators. *ACS Photonics* **2020**, *7*, 2122−2131.

(50) Verbunt, P. P. C.; Sánchez-Somolinos, C.; Broer, D. J.; Debije, M. G. *Anisotropic Light Emissions in Luminescent Solar Concentrators*; Optical Society of America, 2012; Vol. 21, pp 485−493.

(51) Verbunt, P. P. C.; De Jong, T. M.; De Boer, D. K. G.; Broer, D. J.; Debije, M. G. Anisotropic Light Emission from Aligned Luminophores. *Eur. Phys. J.: Appl. Phys.* **2014**, *67*, No. 10201.

(52) Verbunt, P. P. C.; Kaiser, A.; Hermans, K.; Bastiaansen, C. W. M.; Broer, D. J.; Debije, M. G. Controlling Light Emission in Luminescent Solar Concentrators through Use of Dye Molecules Aligned in a Planar Manner by Liquid Crystals. *Adv. Funct. Mater.* **2009**, *19*, 2714−2719.

(53) Moraitis, P.; de Boer, D. K. G.; Prins, P. T.; de Mello Donegá, C.; Neyts, K.; van Sark, W. G. J. H. M. Should Anisotropic Emission or Reabsorption of Nanoparticle Luminophores Be Optimized for Increasing Luminescent Solar Concentrator Efficiency? *Sol. RRL* **2020**, *4*, No. 2000279.

(54) Curto, A. G.; Volpe, G.; Taminiau, T. H.; Kreuzer, M. P.; Quidant, R.; Hulst, N. F. Van. Unidirectional Emission of a Quantum Dot Coupled to a Nanoantenna. *Science* **2010**, *20*, 930−933.

(55) Hanifi, D. A.; Bronstein, N. D.; Koscher, B. A.; Nett, Z.; Swabeck, J. K.; Takano, K.; Schwartzberg, A. M.; Maserati, L.; Vandewal, K.; van de Burgt, Y.; Salleo, A.; Alivisatos, A. P. Redefining Near-Unity Luminescence in Quantum Dots with Photothermal Threshold Quantum Yield. *Science* **2019**, *363*, 1199−1202.

(56) Fang, H.; Battaglia, C.; Carraro, C.; Nemsak, S.; Ozdol, B.; Kang, J. S.; Bechtel, H. A.; Desai, S. B.; Kronast, F.; Unal, A. A.; Conti, G.; Conlon, C.; Palsson, G. K.; Martin, M. C.; Minor, A. M.; Fadley, C. S.; Yablonovitch, E.; Maboudian, R.; Javey, A. Strong Interlayer Coupling in van Der Waals Heterostructures Built from Single-Layer Chalcogenides. *Proc. Natl. Acad. Sci.* **2014**, *111*, 6198−6202.

(57) Capretti, A.; Lesage, A.; Gregorkiewicz, T. Integrating Quantum Dots and Dielectric Mie Resonators: A Hierarchical Metamaterial Inheriting the Best of Both. *ACS Photonics* **2017**, *4*, 2187−2196.

(58) Vaskin, A.; Liu, S.; Addamane, S.; Vabishchevich, P. P.; Yang, Y.; Balarishnan, G.; Sinclair, M. B.; Pertsch, T.; Brener, I.; Staude, I. Manipulation of Quantum Dot Emission with Semiconductor Metasurfaces Exhibiting Magnetic Quadrupole Resonances. *Opt. Express* **2021**, *29*, 5567.

(59) Steiner, M. A.; Geisz, J. F.; García, I.; Friedman, D. J.; Duda, A.; Kurtz, S. R. Optical Enhancement of the Open-Circuit Voltage in High Quality GaAs Solar Cells. *J. Appl. Phys.* **2013**, *113*, No. 123109.

(60) Green, M. A. Radiative Efficiency of State-of-the-art Photovoltaic Cells. *Prog. Photovoltaics* **2012**, *20*, 472−476.

(61) Shockley, W.; Queisser, H. J. Detailed Balance Limit of Efficiency of P-n Junction Solar Cells. *J. Appl. Phys.* **1961**, *32*, 510−519.

(62) Sandhu, S.; Yu, Z.; Fan, S. Detailed Balance Analysis of Nanophotonic Solar Cells. *Opt. Express* **2013**, *21*, 1209.

(63) Slooff, L. H.; Kinderman, R.; Burgers, A. R.; Büchtemann, A.; Danz, R.; Meyer, T. B.; Chatten, A. J.; Farell, D.; Barnham, K. W. J.; van Roosmalen, J. A. M. The Luminescent Concentrator Illuminated. *Photonics Sol. Energy Syst.* **2006**, *6197*, No. 61970K.

(64) Rau, U.; Einsele, F.; Glaeser, G. C. Efficiency Limits of Photovoltaic Fluorescent Collectors. *Appl. Phys. Lett.* **2005**, *87*, 1−3.

(65) Glaeser, G. C.; Rau, U. Collection and Conversion Properties of Photovoltaic Fluorescent Collectors with Photonic Band Stop Filters. *Proc. SPIE* **2006**, *6197*, 61970L.

(66) Bronstein, N. D.; Yao, Y.; Xu, L.; O'Brien, E.; Powers, A. S.; Ferry, V. E.; Alivisatos, A. P.; Nuzzo, R. G. Quantum Dot Luminescent Concentrator Cavity Exhibiting 30-Fold Concentration. *ACS Photonics* **2015**, *2*, 1576−1583.

(67) Şahin, D.; Ilan, B.; Kelley, D. F.; Sahin, D.; Ilan, B.; Kelley, D. F. Monte-Carlo Simulations of Light Propagation in Luminescent Solar Concentrators Based on Semiconductor Nanoparticles. *J. Appl. Phys.* **2011**, *110*, No. 033108.

(68) Sadeghi, S.; Melikov, R.; Bahmani Jalali, H.; Karatum, O.; Srivastava, S. B.; Conkar, D.; Firat-Karalar, E. N.; Nizamoglu, S. Ecofriendly and Efficient Luminescent Solar Concentrators Based on Fluorescent Proteins. *ACS Appl. Mater. Interfaces* **2019**, *11*, 8710−8716.

(69) Verbunt, P. P. C.; Sánchez-Somolinos, C.; Broer, D. J.; Debije, M. G. Anisotropic Light Emissions in Luminescent Solar Concentrators−Isotropic Systems. *Opt. Express* **2013**, *21*, A485.